JACS
JOURNAL OF THE AMERICAN CHEMICAL SOCIETY
Article
pubs.acs.org/JACS

Benchmarking Heterogeneous Electrocatalysts for the Oxygen Evolution Reaction

Charles C. L. McCrory,*[,§] Suho Jung,[§] Jonas C. Peters,*[,§,†] and Thomas F. Jaramillo*[,§,‡]

[§]Joint Center for Artificial Photosynthesis and [†]Division of Chemistry and Chemical Engineering, California Institute of Technology, Pasadena, California 91125, United States

[‡]Department of Chemical Engineering, Stanford University, Stanford, California 94305, United States

Supporting Information

ABSTRACT: Objective evaluation of the activity of electrocatalysts for water oxidation is of fundamental importance for the development of promising energy conversion technologies including integrated solar water-splitting devices, water electrolyzers, and Li-air batteries. However, current methods employed to evaluate oxygen-evolving catalysts are not standardized, making it difficult to compare the activity and stability of these materials. We report a protocol for evaluating the activity, stability, and Faradaic efficiency of electrodeposited oxygen-evolving electrocatalysts. In particular, we focus on methods for determining electrochemically active surface area and measuring electrocatalytic activity and stability under conditions relevant to an integrated solar water-splitting device. Our primary figure of merit is the overpotential required to achieve a current density of 10 mA cm^{-2} per geometric area, approximately the current density expected for a 10% efficient solar-to-fuels conversion device. Utilizing the aforementioned surface area measurements, one can determine electrocatalyst turnover frequencies. The reported protocol was used to examine the oxygen-evolution activity of the following systems in acidic and alkaline solutions: CoO_x, CoPi, $CoFeO_x$, NiO_x, $NiCeO_x$, $NiCoO_x$, $NiCuO_x$, $NiFeO_x$, and $NiLaO_x$. The oxygen-evolving activity of an electrodeposited IrO_x catalyst was also investigated for comparison. Two general observations are made from comparing the catalytic performance of the OER catalysts investigated: (1) in alkaline solution, every non-noble metal system achieved 10 mA cm^{-2} current densities at similar operating overpotentials between 0.35 and 0.43 V, and (2) every system but IrO_x was unstable under oxidative conditions in acidic solutions.

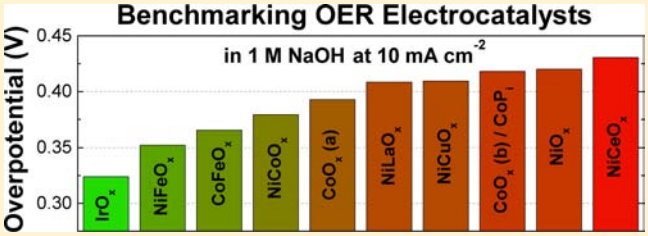

INTRODUCTION

The efficient electrochemical conversion of H_2O to H_2 and 1/2 O_2 catalyzed by materials comprised of earth-abundant elements is of fundamental importance to solar-fuels devices.[1−10] Integrated solar water-splitting devices that couple light-capturing semiconductors with electrocatalysts to efficiently split water show particular promise as a means of direct production of fuels from sunlight.[9] Identifying efficient electrocatalysts for the oxygen evolution reaction (OER) remains a key challenge in the production of solar fuel generators,[6,11,12] and methods for rapidly screening the OER activity of various metal oxides have recently been reported in the context of combinatorial catalyst synthesis.[13,14] However, objective evaluation of the efficiency of OER catalysts is complicated by the lack of standardization both in the measurement and reporting of electrocatalytic data. Typical OER catalysts are deposited on a variety of different substrates, and their electrocatalytic activity is measured at a range of pH values, temperatures, and electrolyte compositions and concentrations, making it difficult to compare the performance and stability of different materials. As such, the development and implementation of a benchmarking methodology to test the electrocatalytic efficiency of materials for OER remain a fundamental challenge in solar fuels research.

In the case of components for commercial devices such as photovoltaic cells and polymer-electrolyte membrane fuel cells (PEMFCs), widely accepted testing protocols and figures of merit exist.[15−17] For instance, one figure of merit that has been used for inexpensive Pt-free oxygen reduction catalysts for PEMFCs is the operating current per cm^3 of catalyst material at a fixed overpotential in acidic water at elevated temperature.[15] In this example, the catalyst testing conditions are dictated by the operating conditions necessary for automotive PEMFCs.[15,18] While the purpose and operating conditions for PEMFCs are significantly different than those for solar water-splitting devices, the testing protocols developed for PEMFCs and other commercial devices nevertheless provide inspiration in the development of a benchmarking methodology for electrocatalysts for solar water-splitting devices.

Herein we report a procedure for evaluating the activity, stability, and electrochemically active surface area for heterogeneous OER catalysts under standard conditions shown in Figure 1. In particular, the electrochemically active surface area (ECSA) of each catalyst is estimated from measurements of the double-layer capacitance; the activity

Received: July 11, 2013
Published: October 30, 2013

dx.doi.org/10.1021/ja407115p | J. Am. Chem. Soc. 2013, 135, 16977−16987

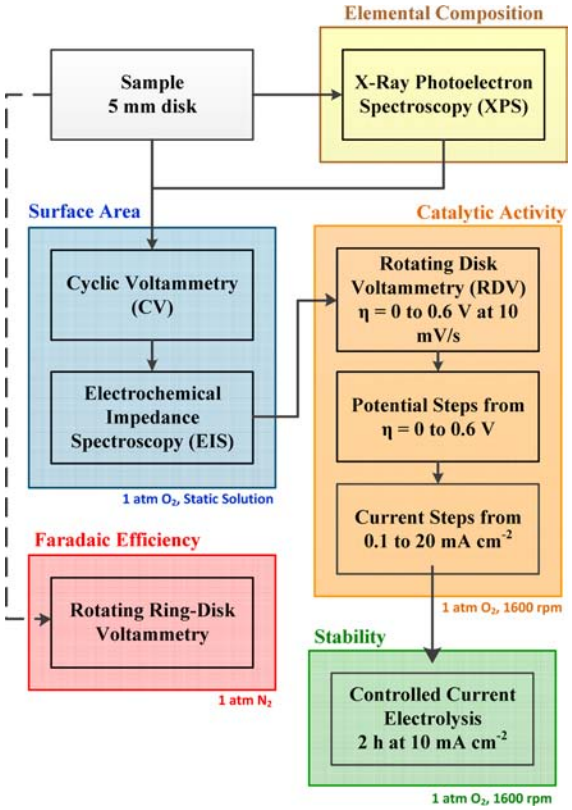

Figure 1. Protocol for measuring the electrochemically active surface area, catalytic activity, stability, and Faradaic efficiency of heterogeneous electrocatalysts for OER.

and stability of each catalyst material are measured using a combination of voltammetry, chronoamperometry, and chronopotentiometry; and the Faradaic efficiency of each material is determined using a rotating ring-disk electrode (RRDE) apparatus. This procedure was developed to meet two specific criteria: (1) to use standard electrochemical procedures and equipment easily accessible to a typical researcher in the field of electrocatalysis, and (2) to minimize the time and number of experiments necessary to evaluate a catalyst's activity and short-term stability. This latter criterion is important to facilitate the screening of large numbers of catalyst materials. The relevant figure of merit is the overpotential required to achieve 10 mA cm^{-2} current density per geometric area at ambient temperature and 1 atm O_2. This is approximately the current density expected at the anode in a 10% efficient solar water-splitting device under 1 sun illumination.[9,19,20]

The protocol outlined above has been used to evaluate and compare the activity and stability of a variety of electrodeposited catalysts for OER under conditions relevant to an integrated solar water-splitting device. A representative sampling of electrodeposited Ni- and Co-based metal oxide catalysts was chosen for initial evaluation (Table 1).[21−23,26−28] Each system was electrodeposited onto an inert, glassy carbon (GC) electrode and studied in aqueous solutions of 1 M NaOH and 1 M H_2SO_4. Glassy carbon was chosen as the electrode support due to its relative inactivity for OER at moderate overpotentials.[29] 1 M NaOH and 1 M H_2SO_4 were chosen as the alkaline and acidic electrolytes because their respective worldwide production volumes greatly exceed those of any other strong acids and bases,[30] making them likely candidates for use as electrolytes in solar fuel devices.[31] The electrocatalytic efficiency of an IrO_x standard[25] and the GC background were also investigated.

EXPERIMENTAL SECTION

Materials. Materials were purchased in the grade indicated and used as received. Ammonium hydroxide (NH_4OH, BioUltra), ammonium perchlorate (NH_4ClO_4, 99.999%), ammonium sulfate ($(NH_4)_2SO_4$, 99.999%), boric acid (H_3BO_3, BioUltra), cobalt(II) nitrate hexahydrate ($Co(NO_3)_2{\cdot}6\ H_2O$, 99.999%), copper(II) sulfate pentahydrate ($CuSO_4{\cdot}5\ H_2O$, 99.995%), nickel(II) nitrate hexahydrate ($Ni(NO_3)_2{\cdot}6\ H_2O$, 99.999%), nickel(II) sulfate hexahydrate ($NiSO_4{\cdot}6\ H_2O$, 99.99%), iron(II) sulfate heptahydrate ($FeSO_4{\cdot}7\ H_2O$, ACS 99%), potassium carbonate (K_2CO_3, 99.995%), potassium hexachloroiridate(IV) dihydrate ($K_2IrCl_6{\cdot}2\ H_2O$, 99.99%), sodium

Table 1. Catalyst Materials Investigated along with Their Deposition Solutions and Conditions

catalyst	deposition solution (in 40 mL H_2O)	deposition conditions
CoO_x-(a)[21]	0.202 g $CoSO_4{\cdot}7\ H_2O$, 0.164 g NH_4ClO_4, NH_4OH to pH 6.8	cathodic deposition at −50 mA cm^{-2} for 30 s[a], 1200 rpm
CoO_x-(b) ("CoPi")[22,23]	0.006 g $Co(NO_3)_2{\cdot}6\ H_2O$, 0.438 g $Na_2HPO_4{\cdot}2\ H_2O$, 0.240 g $NaH_2PO_4{\cdot}2\ H_2O$, pH 7	anodic deposition at 1.05 V vs SCE for 8 h in quiescent solution
$CoFeO_x$[21]	0.112 g $CoSO_4{\cdot}7\ H_2O$, 0.100 g $FeSO_4{\cdot}7\ H_2O$, 0.141 g NH_4ClO_4, NH_4OH to pH 5.4	cathodic deposition at −27.5 mA cm^{-2} for 30 s[a], 1200 rpm
IrO_x[24,25]	see Experimental section	anodic deposition at 1.40 V vs SCE for 600 s in ice bath, 1200 rpm
NiO_x[26]	1.047 g $Ni(NO_3)_2{\cdot}6\ H_2O$	cathodic deposition at −16 mA cm^{-2} for 10 s, 400 rpm
$NiCeO_x$[26]	1.047 g $Ni(NO_3)_2{\cdot}6\ H_2O$, 0.174 g $Ce(NO_3)_3{\cdot}6\ H_2O$	cathodic deposition at −16 mA cm^{-2} for 10 s, 400 rpm
$NiCoO_x$[27]	2.63 g $NiSO_4{\cdot}6\ H_2O$, 2.81 g $CoSO_4{\cdot}7\ H_2O$, 6.44 g $Na_2SO_4{\cdot}10\ H_2O$, 1.24 g H_3BO_3	cathodic deposition at −50 mA cm^{-2} for 15 min, 400 rpm
$NiCuO_x$[28]	0.095 g $NiSO_4{\cdot}6\ H_2O$, 0.090 g $CuSO_4{\cdot}5\ H_2O$, 0.132 g $(NH_4)_2SO_4$	Cathodic deposition at −47 mA cm^{-2} for 50 s[a], 1200 rpm
$NiFeO_x$[21]	0.095 g $NiSO_4{\cdot}6\ H_2O$, 0.100 g $FeSO_4{\cdot}7\ H_2O$, 0.117 g $(NH_4)_2SO_4$, NH_4OH/H_2SO_4 to pH 2.5	cathodic deposition at −50 mA cm^{-2} for 50 s[a], 1200 rpm
$NiLaO_x$[26]	1.047 g $Ni(NO_3)_2{\cdot}6\ H_2O$, 0.173 g $La(NO_3)_3{\cdot}6\ H_2O$	cathodic deposition at −16 mA cm^{-2} for 10 s, 400 rpm

[a]The reported cathodic deposition current density of these materials on Pt discs was −250 mA cm^{-2}. The large reported deposition current density may be due to background H_2 evolution by the Pt substrate. We were unable to attain this current density when depositing onto GC disks and instead deposited at the current densities listed.

dx.doi.org/10.1021/ja407115p | J. Am. Chem. Soc. 2013, 135, 16977−16987

phosphate dibasic dihydrate ($Na_2HPO_4{\cdot}2\ H_2O$, BioUltra), sodium phosphate monobasic dihydrate ($NaH_2PO_4{\cdot}2\ H_2O$, BioUltra), and sodium hydroxide (NaOH, BioUltra) were purchased from Sigma-Aldrich. REacton grade cerium(III) nitrate hexahydrate ($Ce(NO_3)_3{\cdot}6\ H_2O$, 99.99%), cobalt(II) sulfate heptahydrate ($CoSO_4{\cdot}7\ H_2O$, 99.999%), and lanthanum(III) nitrate hexahydrate ($La(NO_3)_3{\cdot}6\ H_2O$, 99.999%) were purchased from Alfa Aesar. TraceMetal grade 98% sulfuric acid (H_2SO_4) was purchased from Fisher Scientific. All water used was first purified by a Thermo Scientific Barnstead Nanopure water purification system (18.2 MΩ·cm resistivity). Oxygen (O_2, Alphagaz-1 grade 99.999%) and argon (Ar, Alphagaz-1 grade 99.999%) were purchased from Air Liquide. Nitrogen (N_2) was bleed-off gas from a liquid nitrogen source.

Analytical Equipment. All activity, stability, and surface area measurements were conducted with a Bio-Logic SP200 potentiostat/galvanostat with a built-in electrochemical impedance spectroscopy (EIS) analyzer or a Bio-Logic VMP3 multichannel potentiostat/galvanostat with a built-in EIS analyzer. The working electrodes were 5 mm diameter disk electrodes mounted in a Pine Instrument Company E6-series ChangeDisk rotating disk electrode assembly in an MSR rotator. In the case of rotating ring-disk electrode voltammetry, the 5 mm disk working electrode was instead mounted in a Pine Instrument Company E6-series Pt ChangeDisk rotating ring-disk electrode assembly. The auxiliary electrodes were carbon rods (99.999%, Alfa Aesar), and the reference electrode was a commercial saturated calomel electrode (SCE) (CH-Instruments) that was externally referenced to a solution of ferrocene monocarboxylic acid (Sigma-Aldrich) in a 0.2 M phosphate buffer at pH 7 (0.284 V vs SCE).[32] Data were recorded using the Bio-Logic EC-Lab and EC-Lab Express software packages.

X-ray photoelectron spectroscopy (XPS) analysis was conducted using a Surface Science Instruments M-probe spectrometer with a monochromatic 1486.6 eV Al Kα X-ray line source directed 35° with respect to the sample surface. The spectrometer was controlled by ESCA25 Capture software (version 5.01.04, Service Physics). Spectra were collected with a hemispherical electron analyzer mounted at an angle of 35° with respect to the sample surface. The sample chamber was maintained at $<5 \times 10^{-9}$ Torr. Low-resolution survey scans were acquired with a 800 μm spot size between the binding energies of 1−1050 eV. Higher-resolution scans with a resolution of ∼0.8 eV were collected between 270 and 340 eV. Analysis of the spectra was done using the CasaXPS Version 2.3.15 software package.

Electrode Preparation. Catalysts were deposited onto 5 mm diameter, 4 mm thick Sigradur G glassy carbon (GC) disks (HTW Hochtemperatur-Werkstoff GmbH). Prior to deposition, the GC disks were first polished with 600 grit Carbimet SiC grinding paper (Buehler) on a Struers LaboPol-5 polishing wheel at 200 rpm for 2 min, then sonicated for 5 min each in pure water, acetone, isopropanol, and again in pure water.

In addition to GC, a 5 mm diameter Pt disk electrode (Pine Instrument Company) was prepared for surface area studies, and 5 mm diameter Ni disk electrodes (cut from Ni rod, Alfa Aesar, 99.995%) were prepared as electrocatalyst surfaces and as additional substrates for $NiCeO_x$ electrodeposition. The disks were sequentially polished with 9, 6, 3, 1, and 0.1 μm MetaDi Supreme diamond slurries (Buehler) with an MD-Floc synthetic nap polishing pad (Struers) on a Struers LaboPol-5 polishing wheel at 150 rpm for several seconds, then sonicated for 5 min each in pure water, acetone, isopropanol, and again in pure water. Sputtered Ni surfaces were prepared as an electrode surface from a Ni target (99.95%, ACI Alloys). The catalyst layer was sputtered onto a polished GC disk from an RF source at 150 W at room temperature under a constant flow of 20 sccm Ar while maintaining an overall pressure of 8.5 mtorr for 35 min.

The deposition conditions for each catalyst were based on literature preparations and are outlined in Table 1. Each electrodeposition was conducted in a 100 mL cell with 40 mL of deposition solution, and the auxiliary electrode was separated from the working and reference electrodes in a separate auxiliary chamber by a fine-porosity glass frit (Bioanalytical Systems Inc.). pH measurements of electrodeposition solutions were conducted with a VWR Symphony multiparameter meter with a Thermo Scientific Orion refillable Ag/AgCl pH electrode filled with Orion Ag/AgCl reference electrode filling solution. The pH meter was calibrated with a 5-point calibration curve between pH 1.68 and 12.45.

For the deposition of IrO_x,[24,25] 0.0580 g K_2IrCl_6 was added to 50 mL of 0.1 M NaOH solution at pH 13 to form a 2.4 mM solution. The solution was heated to 90 °C for 20 min, and the resulting blue solution was placed in an ice bath and allowed to cool. After the solution temperature reached ∼2 °C, 0.8 mL of 3 M HNO_3 was rapidly added to the cold IrO_x deposition solution.[25] The resulting dark-blue solution was stirred for 80 min in an ice bath. The cold solution was used for the deposition according to the conditions reported in Table 1, and the deposition solution was stored in a refrigerator at 5 °C between depositions for up to one week.

Electrochemical Characterization. All activity, stability, and surface area measurements were conducted in a modified two-chamber U-cell in which the first chamber held the working and reference electrodes in ∼120 mL of solution, and the second chamber held the auxiliary electrode in ∼25 mL of solution. The two chambers were separated by a fine-porosity glass frit. The cell was purged for ∼20 min with O_2 prior to each set of experiments. During static voltammetry measurements, the solution in the first chamber was blanketed under O_2. During rotating disk electrode voltammetry (RDEV) measurements, the solution in the first chamber was continuously bubbled with O_2. The uncompensated resistance of the cell was measured with a single-point high-frequency impedance measurement, and IR drop was compensated at 85% through positive feedback using the Bio-Logic EC-Lab software. Our typical electrochemical cell had R_u = ∼10 Ω in 1 M H_2SO_4 and R_u = ∼20 Ω in 1 M NaOH.

Electrochemical capacitance measurements were determined using cyclic voltammetry (CV)[33] and EIS.[34−36] First, the potential range where there is a non-Faradaic current response was determined from CV. This range is typically a 0.1 V potential window centered on the open-circuit potential (OCP) of the system. CV measurements were conducted in static solution by sweeping the potential across the nonfaradaic region from the more positive to negative potential and back at 8 different scan rates: 0.05, 0.01, 0.025, 0.05, 0.1, 0.2, 0.4, and 0.8 V s^{-1}. The working electrode was held at each potential vertex for 10 s before beginning the next sweep.[37] EIS measurements were conducted in static solution at three points: the two vertices and the midpoint potential of the voltammetry measurements. The amplitude of the sinusoidal wave was 10 mV, and the frequency scan range was from 100 kHz to 100 Hz. EIS spectra were analyzed with the Bio-Logic EC-Lab software package.

The Faradaic efficiency of O_2 production by each catalyst was measured using a RRDE apparatus. The collection efficiency, N, of the rotating ring-disk electrode assembly was independently determined to be N = 19 ± 1% from reducing $K_3Fe(CN)_6$ at a GC electrode and reoxidizing it at the Pt ring. RRDE measurements were conducted in a cell purged for ∼20 min with N_2 and then blanketed with N_2 during the experiment. Since the freshly prepared electrodeposited catalysts are generally derived from cathodic depositions, prior to each RRDE experiment the electrodeposited catalyst was first pre-anodized at 10 mA cm^{-2} for 2 min in 1 M NaOH at 1600 rpm. Before any ring currents were collected, the Pt ring was polished by hand with 1 μm MetaDi Supreme diamond slurry (Buehler) first on a Nylon polishing cloth (Buehler) and then on a Microcloth polishing pad (Buehler), followed by rinsing and ∼1 min sonication in pure water. The disk electrode was then held at open circuit for 2 min, and the ring electrode was held at −0.7 V vs SCE in N_2-saturated 1 M NaOH. This was to establish the background current at the ring electrode. The magnitude of the background currents was typically $|i_{ring}| < 3$ μA. The disk electrode was then subjected to sequential 1 min current steps at 0.5, 1, 2 , 5, and 10 mA cm^{-2} at 1600 rpm in 1 M NaOH, while the ring was held constant at −0.7 V vs SCE.

RESULTS AND DISCUSSION

The general procedure used to evaluate each catalytic material is highlighted in Figure 1. The techniques used to determine

the electrochemically active surface area, electrocatalytic activity, stability, and Faradaic efficiency for each OER catalyst investigated are described in detail below. An important note is that the goal of this benchmarking study is to propose a useful, moderate through-put method for screening a variety of OER catalysts. Each catalyst studied was chosen as representative of broad classes of catalysts. Catalysts were synthesized by electrodeposition, following literature procedures with the possible exception of the electrode support, as outlined in the Experimental section. In this study, GC was the substrate used for all catalysts. We note that the benchmarking protocol reported here was designed specifically for testing OER electrocatalysts under conditions relevant to an integrated solar water-splitting device under 1 sun illumination.

Surface Analysis. The qualitative elemental composition of representative samples for each catalyst was determined using X-ray photoelectron spectroscopy (XPS) (Figures S1−S11). Survey scans from 1 to 1050 eV binding energy were used to confirm the qualitative composition of each sample and to ensure that only the elements expected in each catalyst sample were present. High-resolution scans from 270 to 340 eV binding energy were used to test for photoemission originating from Pt_{4d}, Ir_{4d}, and Ru_{3d}. Other than in the case of IrO_x, no peaks associated with noble metals appeared in the high-resolution scans. We thus suspect no noble metal presence in the electrodeposited catalysts within the ∼0.1 atom % detection limit of XPS.[38,39]

Electrochemically Active Surface Area. The electrochemically active surface area (ECSA) for each system was estimated from the electrochemical double-layer capacitance of the catalytic surface.[33] The electrochemical capacitance was determined using two different methods: (1) by measuring the non-Faradaic capacitive current associated with double-layer charging from the scan-rate dependence of cyclic voltammograms (CVs)[33,37] and (2) from measuring the frequency-dependent impedance of the system using electrochemical impedance spectroscopy (EIS).[34−36]

To measure double-layer charging via CV, a potential range in which no apparent Faradaic processes occur was determined from static CV. This range is typically a 0.1 V potential window centered at the open-circuit potential (OCP) of the system. All measured current in this non-Faradaic potential region is assumed to be due to double-layer charging. The charging current, i_c, is then measured from CVs at multiple scan rates. Examples of CVs of the electrodeposited NiO_x catalyst in a non-Faradaic potential range is shown in Figure 2a. The working electrode was held at each potential vertex for 10 s before beginning the next sweep. The double-layer charging current is equal to the product of the scan rate, ν, and the electrochemical double-layer capacitance, C_{DL}, as given by eq 1.[33,37,40,41]

$$i_c = \nu C_{DL} \tag{1}$$

Thus, a plot of i_c as a function of ν yields a straight line with a slope equal to C_{DL} (Figure 2b). The electrochemical double-layer capacitance measured from the scan-rate dependent CVs for the electrodeposited NiO_x catalyst is C_{DL} = 0.091 mF.

The double-layer capacitance was also measured using EIS in the same non-Faradaic region. A sinusoidal potential is applied to the system and the frequency-dependent complex impedance is measured. An example Nyquist plot of the real and imaginary components of the electrochemical impedance in a non-Faradaic region measured between 100 Hz and 100 kHz

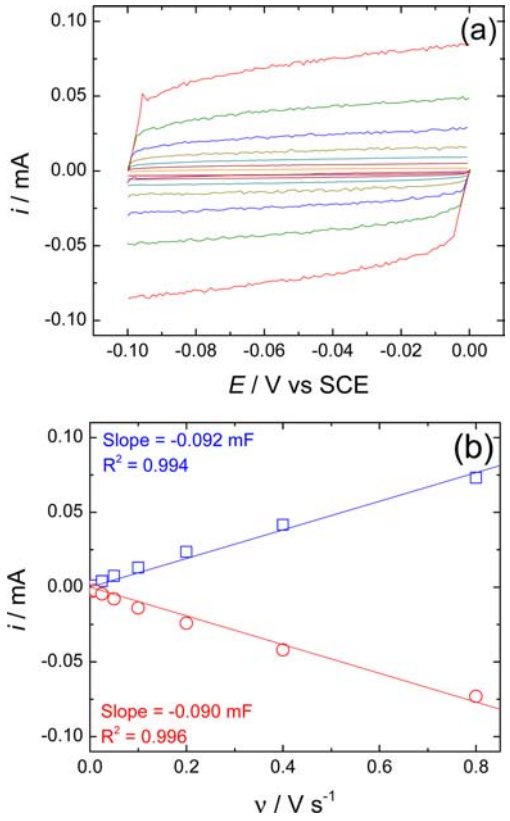

Figure 2. Double-layer capacitance measurements for determining electrochemically active surface area for an electrodeposited NiO_x catalyst from voltammetry in 1 M NaOH. (a) Cyclic voltammograms were measured in a non-Faradaic region of the voltammogram at the following scan rate: (purple line) 0.005, (orange line) 0.01, (dark red line) 0.025, (cyan line) 0.05, (brown line) 0.1, (blue line) 0.2, (green line) 0.4, and (red line) 0.8 V/s. The working electrode was held at each potential vertex for 10 s before the beginning the next sweep. All current is assumed to be due to capacitive charging. (b) The cathodic (red open circle) and anodic (blue open square) charging currents measured at −0.05 V vs SCE plotted as a function of scan rate. The determined double-layer capacitance of the system is taken as the average of the absolute value of the slope of the linear fits to the data.

for an electrodeposited NiO_x catalyst is shown in Figure 3. In the limit of high frequency and under non-Faradaic conditions, the electrochemical system is approximated by the modified Randles circuit shown in the inset of Figure 3, where R_s is the solution resistance, CPE is a constant-phase element related to the double-layer capacitance, and R_{ct} is the charge-transfer resistance from any residual Faradaic processes.[42]

The frequency-dependent impedance of the CPE is given by eq 2:[34,35]

$$Z_{CPE} = \frac{1}{Q_0(i\omega)^{1-\alpha}} \tag{2}$$

where ω is the frequency of the sinusoidal applied potential, $i = (-1)^{1/2}$, Q_0 is a constant with units of F s^{a-1}, and $1 \geq a \geq 0$ is related to the phase angle of the frequency response. For the circuit model used here, it has been suggested that Q_0 is related to C_{DL} according to eq 3.[34,35]

$$C_{DL} = \left[Q_0 \left(\frac{1}{R_s} + \frac{1}{R_{ct}} \right)^{(a-1)} \right]^{1/a} \tag{3}$$

dx.doi.org/10.1021/ja407115p | J. Am. Chem. Soc. 2013, 135, 16977−16987

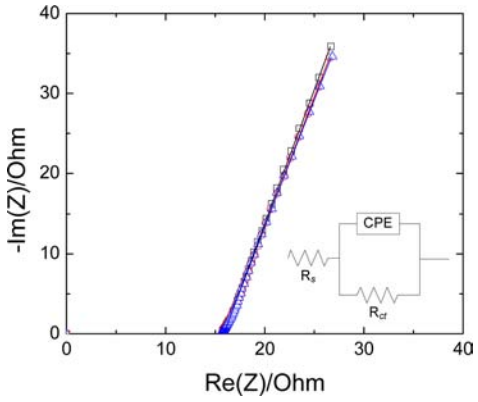

Figure 3. Representative Nyquist plots for an electrodeposited NiO_x catalyst in 1 M NaOH at −0.1 V (black open square), −0.05 V(red open circle), and 0 V (blue open triangle) vs SCE measured from EIS in the frequency range 100 kHz to 100 Hz. These potentials fall in a potential region in which no Faradaic processes are observed. The solid lines are the fits to the data using the simplified Randles circuit shown in the inset.

Note that when $a = 1$, the constant phase element behaves as a pure capacitor and $C_{DL} = Q_0$, and when $a = 0$, the constant phase element behaves as a pure resistor and C_{DL} is undefined. From the EIS measurement of the electrodeposited NiO_x system at $E = -0.05$ V vs SCE shown in Figure 3, $R_s = 15.9$ Ω, $R_{ct} = 11.2$ kΩ, $Q_0 = 0.151$ mF s^{a-1}, and $a = 0.815$. The calculated $C_{DL} = 0.079$ mF. Note that the double-layer capacitance measured by EIS is within 15% of that measured from the scan rate-dependent CVs. In general, we have found that the C_{DL} measured for a given sample by the two methods tend to agree within ±15%.

The ECSA of a catalyst sample is calculated from the double-layer capacitance according to eq 4:

$$\text{ECSA} = \frac{C_{DL}}{C_s} \tag{4}$$

where C_s is the specific capacitance of the sample or the capacitance of an atomically smooth planar surface of the material per unit area under identical electrolyte conditions. While ideally one would synthesize smooth, planar surfaces of each catalyst to measure C_s and estimate ECSA, this is not practical for most electrodeposited systems. However, specific capacitances have been measured for a variety of metal electrodes in acidic and alkaline solutions and typical values reported range between $C_s = 0.015-0.110$ mF cm^{-2} in H_2SO_4[44−53] and $C_s = 0.022-0.130$ mF cm^{-2} in NaOH and KOH solutions.[47,50,52,54−63] For our estimates of surface area, we use general specific capacitances of $C_s = 0.035$ mF cm^{-2} in 1 M H_2SO_4 and $C_s = 0.040$ mF cm^{-2} in 1 M NaOH based on typical reported values.[64] The roughness factor (RF) is calculated by taking the estimated ECSA and dividing by the geometric area of the electrode, 0.195 cm^2. Average ECSA and RF values for each catalyst investigated in this study along with standard deviations from at least three independent measurements are shown in Table 2. Note that the standard deviations are an indication of the precision of the measurements and not necessarily the accuracy of the calculated ECSA and RF.

Because we use a standard value for specific capacitance in our calculations, the error in the accuracy of estimates of ECSA could be as large as a factor of 7 based on the range of reported C_s for metal electrodes in acidic and alkaline electrolyte solutions.[33,41] Moreover, in estimating the ECSA from C_{DL}, we do not take into account other possible contributions to the measured capacitance including pseudocapacitance due to ion adsorption and intercalation or chemical capacitance due to the population of electron trap states. The double-layer capacitance measurements assume that the metal oxide catalysts are equally conductive, which is another potential source of error in these measurements. In general, we believe the ECSA estimates to be accurate within about an order of magnitude, but caution that the values should be considered only as an approximate guide for comparing surface roughness.

As a validation of the proposed benchmarking methods for determining surface area, we have compared the electrochemically active surface area of a Pt disk electrode determined using our protocols to that determined from estimating the amount of adsorbed hydrogen in the H-UPD region of the voltammogram in 1 M H_2SO_4 under 1 atm N_2 (Figures S12−S14), a well-established method for Pt.[33,61,65] The surface area was calculated from the area of the electrochemical peak associated

Table 2. Benchmarking Parameters for Each Catalyst Investigated in 1 M NaOH

catalyst	ECSA/cm^2	RF	$\eta_{t=0}$/V	$\eta_{t=2h}$/V	$j_{g,\eta=0.35\ V}$/mA cm^{-2}	$j_{s,\eta=0.35\ V}$/mA cm^{-2}	ε	reported $\eta_{t=0}$/V
CoO_x-(a)	1.9 ± 0.6	10 ± 3	0.39 ± 0.04	0.42 ± 0.04	0.9 ± 0.3	0.09 ± 0.04	0.94 ± 0.08	0.38[a]
CoO_x-(b) ("CoPi")	5.1 ± 1.7	26 ± 9	0.42 ± 0.02	0.44 ± 0.02	0.4 ± 0.1	0.015 ± 0.006	1.00 ± 0.10	0.43[b] 0.41[c]
$CoFeO_x$	3.6 ± 0.9	19 ± 5	0.37 ± 0.02	0.43 ± 0.03	7 ± 3	0.4 ± 0.2	0.98 ± 0.08	0.34[a]
IrO_x	21 ± 10	105 ± 53	0.32 ± 0.04	1.05 ± 0.20	42 ± 13	0.4 ± 0.2	0.92 ± 0.07	0.32[d] 0.30[e]
NiO_x	1.8 ± 0.5	9 ± 3	0.42 ± 0.02	0.41 ± 0.05	1.1 ± 0.4	0.12 ± 0.05	0.93 ± 0.08	0.42[f]
$NiCeO_x$	3.3 ± 1.2	17 ± 6	0.43 ± 0.03	0.44 ± 0.02	1.6 ± 0.7	0.11 ± 0.07	0.90 ± 0.08	0.28[f]
$NiCoO_x$	5.2 ± 2.1	27 ± 11	0.38 ± 0.03	0.36 ± 0.01	6 ± 3	0.2 ± 0.1	0.92 ± 0.08	0.40[g]
$NiCuO_x$	1.8 ± 0.3	9 ± 2	0.41 ± 0.01	0.44 ± 0.03	1.4 ± 0.6	0.15 ± 0.07	0.95 ± 0.13	0.42[h]
$NiFeO_x$	1.1 ± 0.5	6 ± 3	0.35 ± 0.01	0.38 ± 0.02	15 ± 6	3 ± 2	1.00 ± 0.04	0.29[a]
$NiLaO_x$	1.2 ± 0.3	6 ± 1	0.41 ± 0.03	0.46 ± 0.05	2.5 ± 0.9	0.4 ± 0.2	0.96 ± 0.09	0.36[f]
GC background	1.9 ± 0.9	10 ± 5	1.19 ± 0.03	1.29 ± 0.02	<0.05	<0.005	0.76 ± 0.07	–

[a]Electrodeposited onto Pt and reported at 100 mA cm^{-2} in air saturated 1 M KOH.[21] [b]Electrodeposited onto FTO glass and reported at 10 mA cm^{-2} in 1 M NaOH.[43] [c]Electrodeposited onto FTO glass and reported at 1 mA cm^{-2} in 0.1 M KH_2PO_4/K_2HPO_4 buffer at pH 7.[22] [d]Electrodeposited onto a GC disk and reported at 10 mA cm^{-2} in 0.1 M NaOH.[24,25] [e]Electrodeposited onto a GC disk and reported at 10 mA cm^{-2} in 0.098 M H_2SO_4.[25] [f]Electrodeposited onto Ni substrate and reported at 16 mA cm^{-2} in 1 M KOH.[26] [g]Electrodeposited onto Cu substrate and reported at 10 mA cm^{-2} in 5 M KOH.[27] [h]Electrodeposited onto Ni substrate and reported at 100 mA cm^{-2} in 1 M NaOH at 80 °C.[28]

dx.doi.org/10.1021/ja407115p | J. Am. Chem. Soc. 2013, 135, 16977−16987

with the stripping of the adsorbed hydrogen from the Pt surface and the resulting ECSA = 1.9 cm^2. The surface area of the same Pt electrode in the same solution calculated from CV and EIS using a specific capacitance of 0.035 mF cm^{-2} was ECSA = 2.1 cm^2. The three values agree within ±10%.

Electrocatalytic Activity. The electrochemical properties of each catalyst were investigated using a three-electrode electrochemical cell in a rotating disk electrode configuration. The OER activity was evaluated primarily by rotating disk electrode voltammetry (RDEV) at 0.01 V s^{-1} scan rate and 1600 rpm rotation rate. This scan rate is slow enough to ensure steady-state behavior at the electrode surface, and the rotation rate is sufficiently fast to aid in product removal and limit bubble formation from evolved O_2 at the electrode surface.

An example voltammogram of NiO_x in 1 M NaOH is shown in Figure 4. In addition, each catalyst was investigated by a

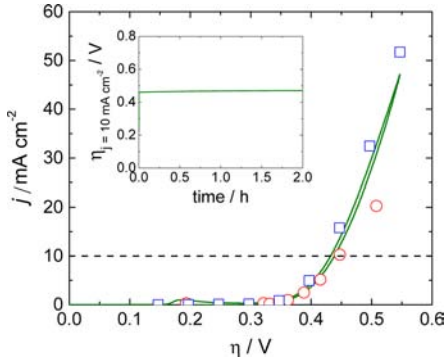

Figure 4. A representative rotating disk voltammogram of the oxygen evolution reaction at an electrodeposited NiO_x catalyst at 0.01 V/s scan rate and 1600 rpm in O_2-saturated 1 M NaOH. The results of 30 s chronopotentiometric steps (red open circle) and chronoamperometric steps (blue open square) are shown for comparison, and the close overlay of the data suggests good approximation of steady-state conditions. The horizontal dashed line at 10 mA cm^{-2} per geometric area is the current density expected for a 10% efficient solar water-splitting device.[9,19,20] The inset is a representative 2 h controlled current electrolysis at 10 mA cm^{-2} per geometric area for the same electrodeposited NiO_x catalyst.

series of controlled-current chronopotentiometric steps and controlled-potential chronoamperometric steps (Figure S15). In such experiments, the current or potential is held constant for 30 s, and the resulting potential−time or current−time profile should decay to a steady-state value at times >2 s.[66,67] Representative steady-state potentials determined from current step measurements and steady-state currents determined from potential step measurements for the electrodeposited NiO_x system are shown as squares and circles in Figure 4 and show good agreement when overlaid with the RDV measurement. The horizontal dashed line is at 10 mA cm^{-2} per geometric area, the current density expected for a 10% efficient solar water-splitting device,[9,19,20] and the overpotential required to achieve this current density, $\eta_{t=0}$, is a convenient figure of merit for electrocatalytic activity.[20,68,69]

Representative rotating disk voltammograms for each material investigated are shown in Figures S16−S25. Average $\eta_{t=0}$ values for each catalyst were calculated from RDV and current step measurements at 10 mA cm^{-2} per geometric area, and the resulting values in 1 M NaOH are reported along with standard deviations measured with at least three independently prepared surfaces in Table 2. Note that, under alkaline conditions, all earth-abundant catalysts investigated in this study show similar activity and achieve 10 mA cm^{-2} per geometric area current densities within a 0.07 V window between η = ∼0.360−0.430 V. For comparison, IrO_x achieves 10 mA cm^{-2} current densities for OER at overpotentials of η = 0.32 ± 0.04 V in 1 M NaOH and η = 0.27 ± 0.3 V in 1 M H_2SO_4. These activities for IrO_x in acid and base are similar to those previously reported for this catalyst.[24,25]

The previously reported overpotentials required to achieve close to 10 mA cm^{-2} for the various catalysts investigated in this study are also reported in Table 2. In general, the overpotentials reported in this study compare well (within ∼15%) to data already reported in the literature for analogous systems. One notable exception is the electrodeposited $NiCeO_x$ catalyst. This was previously reported as an electrodeposited catalyst on a nickel electrode with an overpotential of 0.28 V required to achieve 16 mA cm^{-2} for OER.[26] This overpotential is significantly lower than the measured overpotential of 0.43 V reported in this study to achieve 10 mA cm^{-2} for a $NiCeO_x$ catalyst deposited onto a GC electrode. This discrepancy suggests that the substrate may play a role in the activity of the $NiCeO_x$ catalyst. For comparison, $NiCeO_x$ was deposited onto a Ni electrode, and the overpotential required to achieve 10 mA cm^{-2} current density was measured to be $\eta_{t=0\ h}$ = 0.30 V, which is consistent with the previously reported activity of $NiCeO_x$ on Ni substrates.[26] However, the operating overpotential required to achieve 10 mA cm^{-2} current density changes to η = 0.35 V over the course of several minutes and then is stable at η = 0.35 for at least 2 h (Figure S28).

Because the focus of this study is to establish a benchmarking protocol, the activity of only a representative sampling of electrodeposited catalysts was thoroughly investigated. However, the methodology presented here should be applicable to any heterogeneous electrocatalytic system. As an illustration of this, we also investigated the activity of a sputtered Ni film on GC and a solid Ni disk electrode in 1 M NaOH. These metallic Ni surfaces are oxidized to a NiO_x material at potentials required for OER.[70,71] Both surfaces show roughly equivalent activity compared to the electrodeposited NiO_x system (Figures S26−S27).

Another activity metric sometimes reported in the electrocatalysis literature is the specific activity at a given overpotential. The definition of specific activity can vary from study to study—it may refer to either the specific current density per catalyst surface area (j_s)[15,72] or the catalytic turnover frequency (TOF). In turn, the TOF may refer to the rate of electron delivery per surface metal atom per second[15] or the rate of product molecules evolved per surface metal atom,[73,74] per total metal atoms including subsurface metal,[75,76] or per electrochemically active surface site.[24,37,77] In general, a catalyst's specific activity can be useful when attempting to compare the intrinsic activity of catalysts with different surface areas or loadings. However, due to the various definitions of specific activity used in the literature, it is important that one be transparent when determining and reporting this parameter. There would be a clear benefit to standardizing how such specific activities are reported.

As an illustrative exercise, here we determine the specific current density of each catalyst investigated. The method employed was chosen because it uses easily measured parameters and requires little knowledge of the catalyst surface structure or active site density. The specific current density, j_s, is calculated by dividing the current density per geometric area at

dx.doi.org/10.1021/ja407115p | J. Am. Chem. Soc. 2013, 135, 16977−16987

a given overpotential, j_g, by the roughness factor of the surface as shown in eq 5.

$$j_s = \frac{j_g}{RF} \quad (5)$$

The average current density per geometric area at $\eta = 0.35$ V, $j_{g,\eta=0.35\ V}$, and the corresponding specific activity, $j_{s,\eta=0.35\ V}$, are shown in Table 2 for each catalyst investigated. The choice of $\eta = 0.35$ V is based on previously reported device models that suggest a 10% efficient solar water-splitting device should operate at 10 mA cm^{-2} with a maximum of ~0.45 V overpotential for OER and HER combined.[9,19,78] Assuming a 0.1 V overpotential for HER leaves 0.35 V overpotential available for OER catalysis. Standard deviations from at least three experiments with identically prepared samples are reported for each $j_{g,\eta=0.35\ V}$, and standard errors calculated from the standard deviations in the RF and $j_{g,\eta=0.35\ V}$ are reported for each $j_{s,\eta=0.35\ V}$. Note that in the case of j_s, the standard errors reported are measures of error in precision. Due to the inaccuracies inherent in determining ECSA and RF, we caution that the j_s values reported should be considered only as an approximate guide for comparing specific activity and do not supplant $\eta_{t=0}$ as the primary figure of merit for catalyst activity.

Electrocatalytic Stability. The short-term stability of each material under catalytic conditions was determined using controlled-current electrolysis. The catalyst material was held at a constant current density of 10 mA cm^{-2} per geometric area for 2 h at a constant 1600 rpm rotation rate, while the operating potential was measured as a function of time. A representative controlled current electrolysis for NiO_x in 1 M NaOH is shown in the inset of Figure 4 (for other systems, see Figures S16–S25), and the average overpotential required to achieve 10 mA cm^{-2} per geometric area after 2 h of constant electrolysis, $\eta_{t=2\ h}$, is reported for each catalyst along with standard deviations measured with at least three independently prepared surfaces in Table 2. If $\eta_{t=0}$ and $\eta_{t=2\ h}$ are the same, then that is evidence that the catalyst is stable under the operating conditions for at least a 2 h period. However, if $\eta_{t=2\ h} > \eta_{t=0}$, then that is evidence of catalyst deactivation over time. Note that the stability measurement used in this study does not distinguish whether the deactivation mechanism is due to corrosion, material degradation, surface passivation, or other processes.

In 1 M NaOH, most catalysts investigated appear stable under operating conditions as the overpotential shifts <0.03 V during the 2 h controlled potential electrolysis at 10 mA cm^{-2} per geometric area. However, two catalysts that do show appreciable shifts in operating overpotential during the course of the stability measurement in 1 M NaOH are $CoFeO_x$, and IrO_x. In the case of $CoFeO_x$, slow catalyst dissolution has been previously reported for spinel-type $Fe_xCo_{3-x}O_4$ ($0 < x < 1$) and related catalysts,[79,80] and this may account for the observed loss of catalytic activity over the course of 2 h.

For IrO_x, the overpotential required to achieve 10 mA cm^{-2} increases from η = ~0.32 V to η = ~1.05 V during 2 h of constant polarization. The general instability of IrO_x catalysts in alkaline solutions under oxidizing condition has been previously reported,[81,82] and may be due to the oxidation of the surface IrO_x to water-soluble IrO_4^{2-} or other solvated Ir(VI) ions.[43,83] If this were the case, one might expect an electrode with a higher IrO_x loading to maintain a more constant overpotential over the 2 h experiment. As a simple test, a higher loading IrO_x catalyst was deposited under standard conditions from a solution prepared with the much higher concentration of 16.1 mM K_2IrCl_6. As expected, this catalyst shows a less drastic change in overpotential, achieving 10 mA cm^{-2} with η = ~0.41 V after 2 h constant polarization (Figure S29), suggesting that activity loss may be due to loss of material.

Controlled current electrolyses for each catalyst in 1 M H_2SO_4 were also investigated. The IrO_x system shows a stable operating overpotential at 10 mA cm^{-2}, changing negligibly from $\eta = 0.27 \pm 0.03$ V to 0.30 ± 0.02 over a 2 h time period. For every other catalyst investigated there is a dramatic increase in the operating potential within only minutes to $\eta = 1.1$ V. Not coincidently, $\eta_{t=2\ h} = 1.11 \pm 0.02$ V is the overpotential at which the bare GC background reaches 10 mA cm^{-2} under these conditions, suggesting that the non-noble metal catalysts investigated here are not stable in acidic solutions under oxidizing conditions and that the current density observed is likely arising from the GC substrate itself.

The stability measurement protocol outlined above is useful as a rapid, preliminary screen of catalyst durability. However, it is important to note that a catalyst that shows good 2 h stability may not show the same stability over longer periods of time. The stability measurements outlined here should be augmented by other long-term stability tests for more in-depth studies of promising catalysts. Moreover, additional experiments to study changes in catalyst composition, the mass of the material, and catalyst surface area would be useful complements to the short-term stability measurements proposed here and should be considered as additional studies for promising materials.

Faradaic Efficiency. A RRDE apparatus was used to confirm the formation of O_2 by each catalyst. RRDE allows for the study of water oxidation at a central electrode disk and the collection of the dissolved O_2 produced at a surrounding Pt-ring electrode. The disk electrode is subjected to sequential 1 min current steps from 0.1 to 10 mA cm^{-2} at a constant rotation rate of 1600 rpm under 1 atm N_2. The dissolved O_2 generated at the disk electrode is then swept across the surrounding Pt ring electrode, which is held at a constant potential $E = -0.7$ V vs SCE to rapidly reduce O_2 to H_2O_2 (Figure S30). Representative disk and ring currents for the electrodeposited NiO_x catalyst system in 1 M NaOH are shown in Figure 5. The Faradaic efficiency was measured from the ring current collected while the disk electrode was held at a constant 1 mA cm^{-2} current density per geometric area; this current density is sufficiently large to ensure appreciable O_2 production but sufficiently small to minimize local saturation and bubble formation at the disk electrode. The Faradaic efficiency of the OER system, ε, is proportional to the ratio of the ring current to the disk current and is given by eq 6:

$$\varepsilon = \frac{2i_r}{i_d N} \quad (6)$$

where i_r is the measured ring current, $i_d = 1.95$ mA is constant disk current for a 0.195 cm^2 disk electrode, and $N = 0.19$ is the collection efficiency for the RRDE.

The mean Faradaic efficiency measured for three independently prepared samples for each catalyst is shown in Table 2 with standard deviations. In general, $\varepsilon \geq 0.9$ for the catalysts investigated in 1 M NaOH. The low Faradaic efficiency for oxygen production by GC may be due to oxidative degradation of the carbon surface. Note that small errors in the ring current and collection efficiency can lead to relatively large errors in ε, which may contribute to the standard deviations of $\sim \pm 0.1$ in the reported measurements. RRDE measurements are useful

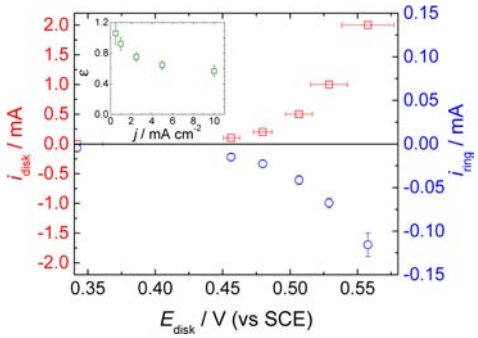

Figure 5. RRDE measurements for the OER by an electrodeposited NiO_x in 1 M NaOH at 1600 rpm rotation rate under 1 atm N_2. The disk electrode was subjected to a series of current steps, and the operating potential was measured. The dissolved oxygen generated at the disk was then reduced by 2 electrons at the surrounding Pt ring electrode. The inset shows a plot of the ratio of the ring and disk current normalized for collection efficiency and the number of electrons in the ring and disk reactions as a function of the disk current. Note that at higher disk currents, the measured current ratio deviates from the expected value of 1. This is likely due to local O_2-saturation and bubble formation at the disk electrode at higher current densities; only dissolved O_2 can be collected at the ring electrode. Faradaic efficiency measurements were calculated at i_d = 0.2 mA, which is j_d = 1 mA cm^{-2} per geometric area.

for quickly screening the approximate Faradaic efficiency of large numbers of catalysts but should be augmented by more selective and sensitive techniques for more in-depth studies of promising single catalysts.

Comparing Catalytic Performance. A key challenge in investigating several parameters related to the performance of catalytic materials for water oxidation is determining a graphical method of quickly and efficiently disseminating relevant parameters. While data tables are certainly capable of conveying large amounts of information, they do not necessarily facilitate cross-comparison of large numbers of materials. As a useful alternative, we present the graphical representation for OER in 1 M NaOH and 1 M H_2SO_4 shown in Figure 6. The *x*-axis represents the overpotential required to achieve 10 mA cm^{-2} per geometric area at time t = 0, a measure of catalytic activity. The *y*-axis represents the overpotential required to achieve 10 mA cm^{-2} per geometric area at time t = 2 h, a measure of catalyst stability. The diagonal dashed line is the expected response for a stable catalyst; materials whose points on this plot deviate from that line show catalyst deactivation (or activation) over time. The color of the each point is related to the roughness factor of the catalyst with a bin size of 1 order of magnitude with light green representing RF = 1 and dark red representing RF > 10^3. The size of each point is inversely proportional to the standard deviation in the ECSA measurement. Since the ideal catalyst will have a low overpotential, be stable over time, and have high specific activity (or low surface area), the best catalyst materials for OER will be positioned toward the bottom left corner of the comprehensive plots and should appear light green in color. Note that there is a break in each axis at 0.5 V, and there is a scale change following this break for values >0.5 V. Catalysts that operate at 10 mA cm^{-2} with overpotentials >0.5 V lie outside the area of interest, but their activity and stability measurements are included in this gray shaded region for completeness.

One key observation prominently illustrated in Figure 6 is that no non-noble metal catalyst investigated in this study

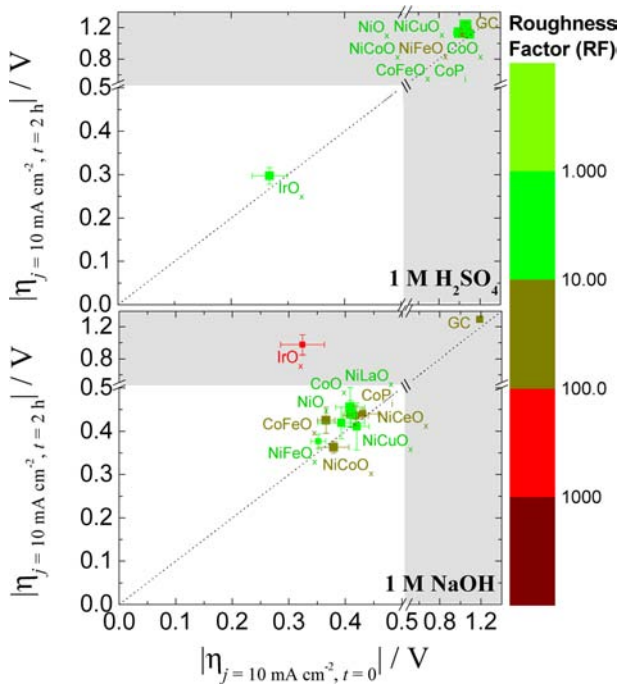

Figure 6. Comprehensive plots of catalytic activity, stability, and electrochemically active surface area for OER electrocatalysts in acidic (top) and alkaline (bottom) solutions. The *x*-axis is the overpotential required to achieve 10 mA cm^{-2} per geometric area at time t = 0. The *y*-axis is the overpotential required to achieve 10 mA cm^{-2} per geometric area at time t = 2 h. The diagonal dashed line is the expected response for a stable catalyst. The color of each point represents the roughness factor of the catalyst with a bin size of 1 order of magnitude with light green representing RF = 1, and dark red representing RF > 10^3. The size of each point is inversely proportional to the standard deviation in the ECSA measurement reported in Table 2. The region of interest for benchmarking is the unshaded white region of the plot where the overpotential required to achieve 10 mA cm^{-2} per geometric area at time t = 0 and 2 h is <0.5 V. There is a break and change in scale in both axes at overpotentials >0.5 V, and the corresponding region of the plot is shown in gray. Catalysts whose activity and stability measurements fall inside this gray area are outside the region of interest for benchmarking, but their activity and stability measurements are included for completeness.

shows appreciable stability under oxidizing conditions in acidic solution—instead, each material degrades to what appears to be a GC background. Although only a comparatively small subset of OER catalysts were investigated, this result nevertheless suggests that significant research targeted toward the discovery of acid-stable non-noble metal OER catalysts must be pursued if any solar-fuels production or other water electrolysis device is to operate under acidic conditions. Another important observation is that, under basic conditions, nearly all earth-abundant catalysts investigated in this study show similar activity achieving 10 mA cm^{-2} per geometric area current densities within a 0.07 V window between η = ~0.360 − 0.430 V. A zoomed-in region of the graphical representation about this potential window in 1 M NaOH is shown in Figure 7.

Among the most promising of the earth-abundant catalysts investigated in 1 M NaOH include $NiFeO_x$ and $NiCoO_x$, which achieve 10 mA cm^{-2} per geometric area current densities at $\eta_{t=0}$ = 0.35 and 0.38 V, respectively, and show good catalyst stability over 2 h. Of the two, $NiFeO_x$ stands out due to its lower surface area and hence higher specific activity; at η = 0.35 V, $NiFeO_x$

dx.doi.org/10.1021/ja407115p | J. Am. Chem. Soc. 2013, 135, 16977−16987

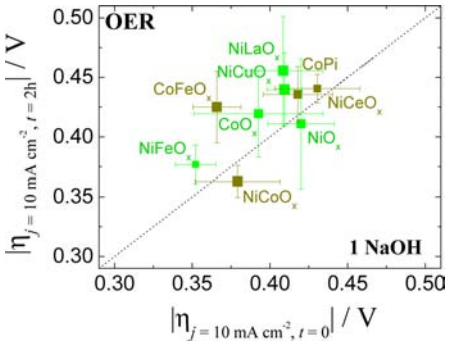

Figure 7. Zoomed-in region of interest for alkaline OER from Figure 6. The *x*-axis is the overpotential required to achieve 10 mA cm^{-2} per geometric area at time t = 0. The *y*-axis is the overpotential required to achieve 10 mA cm^{-2} per geometric area at time t = 2 h. The diagonal dashed line is the expected response for a stable catalyst. The color of each point represents the roughness factor of the catalyst with a bin size of 1 order of magnitude as shown in Figure 6. The size of each point is inversely proportional to the standard deviation in the ECSA measurement reported in Table 2

has a specific current density that is ∼10 times higher than the other non-noble metal catalyst investigated. This suggests $NiFeO_x$ has the highest specific activity of the materials investigated, although it is again important to note the uncertainty inherent in the ECSA and j_s measurements. In addition to $NiFeO_x$ and $NiCoO_x$, $CoFeO_x$ also shows promising activity achieving 10 mA cm^{-2} per geometric area current density at a comparable overpotential of $\eta_{t=0}$ = 0.37 V, but it lacks the stability of the $NiFeO_x$ and $NiCoO_x$ systems.

The electrodeposited single metal NiO_x, CoO_x-(a), and CoO_x-(b) evolve O_2 at 10 mA cm^{-2} per geometric area current densities at only ∼0.05−0.07 V higher overpotential than the $NiFeO_x$ and $NiCoO_x$ systems and also show good catalyst stability over 2 h. Note that while CoO_x-(b) shows the same general activity as NiO_x and CoO_x-(a), its estimated specific activity is ∼6−9 times lower at η = 0.35 V. None of the non-noble metal catalysts investigated approach the activity of IrO_x in 1 M NaOH, which achieves a 10 mA cm^{-2} per geometric area current density at η = 0.32 V in 1 M NaOH, although the catalytic activity of IrO_x decreases significantly over the course of 2 h of constant current electrolysis at 10 mA cm^{-2}.

It is important to note that the benchmarking methodology reported here is proposed as a primary screen in evaluating catalyst activity and stability under conditions relevant to an integrated solar water-splitting device under 1 sun illumination. Other parameters not studied as part of this protocol may be important in catalyst design for specific PEC systems. For instance, the thickness and absorptivity of the OER catalyst may have a profound effect on its performance when integrated with a semiconductor as a photoanode in an integrated solar water-splitting device, and therefore examining these traits may be an important secondary screen.[84] Moreover, an important secondary screen for systems operating at higher current densities, such as PEC systems with concentrated solar, may include testing the electrocatalytic activity at higher current densities. It is worth considering that standard electrochemical methods for studying OER catalysts might be in a mass-transport limited regime when drawing ≥100 mA cm^{-2}, and as such benchmarking catalysts at high current densities may be influenced more by concentration overpotentials rather than by the electrochemical kinetics of the material. Similar considerations should be taken when applying this catalyst benchmarking methodology to other systems.

CONCLUSIONS

A benchmarking protocol for evaluating the activity, stability, electrochemically active surface area, and Faradaic efficiency of heterogeneous OER catalysts under conditions relevant to an integrated solar water-splitting device has been presented. The protocol was used to compare the electrocatalytic performance of 10 heterogeneous OER catalysts deposited onto GC substrates. In addition, a graphical representation of relevant electrocatalytic parameters was developed in order to facilitate the comparison of the electrocatalytic performance for the various OER catalysts.

By systematically comparing a range of OER catalyst materials using identical methods and procedures, several important general observations can be made. First, every non-noble metal catalyst investigated herein showed similar OER activity in 1 M NaOH, achieving 10 mA cm^{-2} current density at overpotentials between 0.35 and 0.43 V. For comparison, an electrodeposited IrO_x catalyst under the same conditions achieved 10 mA cm^{-2} current density at η = 0.32 ± 0.04 V, although IrO_x was unstable during 2 h of constant current electrolysis. This suggests that there is still significant room for improvement in discovering OER catalysts that can operate at high current density and lower overpotential in a stable manner.

Second, only IrO_x showed stability in 1 M H_2SO_4, maintaining 10 mA cm^{-2} current density at η = ∼0.30 V for 2 h of constant current electrolysis. Every non-noble metal catalyst investigated was unstable under oxidative conditions in 1 M H_2SO_4, ultimately exhibiting the same catalytic behavior as the GC substrate. This result highlights the need for non-noble metal acid-stable OER catalysts in order for solar water-splitting devices operating in 1 M H_2SO_4 to be feasible.

As a secondary screen of OER activity, the specific activity of each electrocatalyst was also determined. $NiFeO_x$ showed the highest specific activity, operating at ∼3 mA cm^{-2} per electrochemically active surface area, nearly 10 times higher than the other catalysts. This suggests that $NiFeO_x$ has a higher intrinsic activity compared with the other systems investigated. Specific activity measurements reported using this method should be taken as an approximate guide rather than an absolute value and do not supplant the overpotential required to achieve 10 mA cm^{-2} per geometric area as a primary figure of merit.

We note that the benchmarking protocol reported here is considered a first and important step in evaluating catalyst materials; further testing will be needed to truly establish catalyst feasibility. We also note that this benchmarking protocol was specifically designed for testing OER electrocatalysts under conditions relevant to an integrated solar water-splitting device under 1 sun illumination. Other devices that use OER electrocatalysts such as PEM and alkaline water electrolyzers or integrated water-splitting cells under multiple-sun illumination may have significantly different operating parameters and as such will have different figures of merit and may require different testing methods than those reported here.

ASSOCIATED CONTENT

Supporting Information

X-ray photoelectron spectra; discussion of choice of specific capacitance values; rotating disk voltammograms, chronopotentiometric steps and chronoamperometric steps for electro-

dx.doi.org/10.1021/ja407115p | J. Am. Chem. Soc. 2013, 135, 16977−16987

deposited catalyts; OER activity and stability measurements for $NiCeO_x$ on Ni electrodes; confirmation of 2 e^- reduction of O_2 on Pt ring electrodes at 0.7 V vs SCE and 1600 rpm rotation rate in 1 M NaOH; rotating disk voltammograms, chronopotentiometric steps and chronoamperometric steps for sputtered Ni and commercial Ni disks; discussion regarding the use of Tafel plots for comparing electrocatalysts and benchmarking intermediate pH solutions. This material is available free of charge via the Internet at http://pubs.acs.org.

AUTHOR INFORMATION

Corresponding Author

benchmarking@solarfuelshub.org

Notes

The authors declare no competing financial interest.

ACKNOWLEDGMENTS

This material is based upon work performed by the Joint Center for Artificial Photosynthesis, a DOE Energy Innovation Hub, supported through the Office of Science of the U.S. Department of Energy under award no. DE-SC0004993. We are grateful for the many useful insights we have received regarding this work from various members of the electrochemistry community. In particular, we would like to acknowledge useful discussions with Allen J. Bard, Fred C. Anson, Nathan S. Lewis, Carl A. Koval, Manuel P. Soriaga, and Hans-Joachim Lewerenz. XPS data was collected at the Molecular Materials Research Center of the Beckman Institute of the California Institute of Technology.

REFERENCES

(1) Grätzel, M. *Acc. Chem. Res.* **1981**, *14*, 376−384.
(2) Koelle, U. *New J. Chem.* **1992**, *16*, 157−169.
(3) Bard, A. J.; Fox, M. A. *Acc. Chem. Res.* **1995**, *28*, 141−145.
(4) Turner, J. A. *Science* **2004**, *305*, 972−974.
(5) Lewis, N. S.; Nocera, D. G. *Proc. Natl. Acad. Sci. U.S.A.* **2006**, *103*, 15729−15735.
(6) Lewis, N. S. *Science* **2007**, *315*, 798−801.
(7) Crabtree, G. W.; Dresselhaus, M. S. *MRS Bull.* **2008**, *33*, 421−428.
(8) Gray, H. B. *Nat. Chem.* **2009**, *1*, 7.
(9) Walter, M. G.; Warren, E. L.; McKone, J. R.; Boettcher, S. W.; Mi, Q.; Santori, E. A.; Lewis, N. S. *Chem. Rev.* **2010**, *110*, 6446−6473.
(10) Vesborg, P. C. K.; Jaramillo, T. F. *RSC Advances* **2012**, *2*, 7933−7947.
(11) Eisenberg, R.; Gray, H. B. *Inorg. Chem.* **2008**, *47*, 1697−1699.
(12) Lewis, N. S.; Crabtree, G.; Nozik, A. J.; Wasielewski, M. R.; Alivisatos, A. P. *Basic Research Needs for Solar Energy Utilization*; Department of Energy: Washington, DC, 2005.
(13) Gerken, J. B.; Chen, J. Y. C.; Massé, R. C.; Powell, A. B.; Stahl, S. S. *Angew. Chem., Int. Ed.* **2012**, *51*, 6676−6680.
(14) Smith, R. D. L.; Prévot, M. S.; Fagan, R. D.; Trudel, S.; Berlinguette, C. P. *J. Am. Chem. Soc.* **2013**, *135*, 11580−11586.
(15) Gasteiger, H. A.; Kocha, S. S.; Sompalli, B.; Wagner, F. T. *Appl. Catal., B* **2005**, *56*, 9−35.
(16) Emery, K. A.; Osterwald, C. R. *Sol. Cells* **1986**, *17*, 253−274.
(17) Shrotriya, V.; Li, G.; Yao, Y.; Moriarty, T.; Emery, K.; Yang, Y. *Adv. Funct. Mater.* **2006**, *16*, 2016−2023.
(18) Matsen, D. A.; Bosco, A. D. In *Handbook of Fuel Cells: Fundamentals, Technology and Applications*; Vielstich, W., Lamm, A., Gasteiger, H., Eds.; Wiley: Chichester, U.K., 2003; Vol. 4, p 714−724.
(19) Weber, M. F.; Dignam, M. J. *J. Electrochem. Soc.* **1984**, *131*, 1258−1265.
(20) Gorlin, Y.; Jaramillo, T. F. *J. Am. Chem. Soc.* **2010**, *132*, 13612−13614.
(21) Merrill, M. D.; Dougherty, R. C. *J. Phys. Chem. C* **2008**, *112*, 3655−3666.
(22) Kanan, M. W.; Nocera, D. G. *Science* **2008**, *321*, 1072−1075.
(23) Surendranath, Y.; Dincă, M.; Nocera, D. G. *J. Am. Chem. Soc.* **2009**, *131*, 2615−2620.
(24) Nakagawa, T.; Beasley, C. A.; Murray, R. W. *J. Phys. Chem. C* **2009**, *113*, 12958−12961.
(25) Zhao, Y.; Hernandez-Pagan, E. A.; Vargas-Barbosa, N. M.; Dysart, J. L.; Mallouk, T. E. *J. Phys. Chem. Lett.* **2011**, *2*, 402−406.
(26) Corrigan, D. A.; Bendert, R. M. *J. Electrochem. Soc.* **1989**, *136*, 723−728.
(27) Ho, J. C. K.; Piron, D. L. *J. Appl. Electrochem.* **1996**, *26*, 515−521.
(28) Li, X.; Walsh, F. C.; Pletcher, D. *Phys. Chem. Chem. Phys.* **2011**, *13*, 1162−1167.
(29) Noel, M.; Anantharaman, P. N. *Surf. Coat. Technol.* **1986**, *28*, 161−179.
(30) Bomgardner, M. M. *Chem. Eng. News* **2011**, *89*, 55−63.
(31) Note that the analytical procedures highlighted in this report can be used in any pH condition, including neutral pH. One of the primary challenges in benchmarking systems near pH 7 concerns the choice of buffer and electrolyte. Because the conjugate bases of buffering systems tend to be relatively coordinating, they often specifically adsorb to metals and metal oxides. This can have a profound effect on the activity of a given OER catalyst. We believe that it would be difficult to define "universal" conditions at intermediate pH and that instead catalysts would need to be studied under more than one buffered and perhaps even unbuffered electrolytes. Such a study is beyond the scope of the current manuscript. See the Supporting Information for an expanded discussion.
(32) Liaudet, E.; Battaglini, F.; Calvo, E. J. *J. Electroanal. Chem.* **1990**, *293*, 55−68.
(33) Trasatti, S.; Petrii, O. A. *Pure Appl. Chem.* **1991**, *63*, 711−734.
(34) Orazem, M. E.; Tribollet, B. *Electrochemical Impedance Spectroscopy*; John Wiley & Sons, Inc.: Hoboken, NJ, 2008, p 233−237.
(35) Brug, G. J.; van den Eeden, A. L. G.; Sluyters-Rehbach, M.; Sluyters, J. H. *J. Electroanal. Chem.* **1984**, *176*, 275−295.
(36) Huang, V. M.-W.; Vivier, V.; Orazem, M. E.; Pébère, N.; Tribollet, B. *J. Electrochem. Soc.* **2007**, *154*, C99−C107.
(37) Benck, J. D.; Chen, Z.; Kuritzky, L. Y.; Forman, A. J.; Jaramillo, T. F. *ACS Catalysis* **2012**, *2*, 1916−1923.
(38) Chusuei, C. C.; Goodman, D. W. In *Encyclopedia of Physical Science and Technology*; 3rd ed.; Robert, A. M., Ed.; Academic Press: New York, 2003, p 921−938.
(39) Klauber, C.; Smart, R. S. C. In *Surface Analysis Methods in Materials Science*; 2 ed.; O'Conner, D. J., Sexton, B. A., Smart, R. S. C., Eds.; Springer-Verlag: Berlin, 2003, p 3−65.
(40) Bockris, J. O. M.; Srinivasan, S. *J. Electroanal. Chem.* **1966**, *11*, 350−389.
(41) Boggio, R.; Carugati, A.; Trasatti, S. *J. Appl. Electrochem.* **1987**, *17*, 828−840.
(42) Bard, A. J.; Faulkner, L. R. *Electrochemical Methods: Fundamentals and Applications*; John Wiley & Sons, Inc.: Hoboken, NJ, 2001, p 383−388.
(43) Minguzzi, A.; Fan, F.-R. F.; Vertova, A.; Rondinini, S.; Bard, A. J. *Chem. Sci.* **2012**, *3*, 217−229.
(44) Frumkin, A. N. *J. Res. Inst. Catal., Hokkaido Univ.* **1967**, *15*, 61−83.
(45) Pickering, H. W. *J. Electrochem. Soc.* **1968**, *115*, 690−694.
(46) Rosen, M.; Flinn, D. R.; Schuldiner, S. *J. Electrochem. Soc.* **1969**, *116*, 1112−1116.
(47) Iseki, S.; Ohashi, K.; Nagaura, S. *Electrochim. Acta* **1972**, *17*, 2249−2265.
(48) Turner, M.; Thompson, G. E.; Brook, P. A. *Corros. Sci.* **1973**, *13*, 985−991.
(49) Glarum, S. H.; Marshall, J. H. *J. Electrochem. Soc.* **1979**, *126*, 424−430.

(50) Badawy, W. A.; Gad-Allah, A. G.; Abd El-Rahman, H. A.; Abouromia, M. M. *Surf. Coat. Technol.* **1986**, *27*, 187−196.
(51) Reid, J. D.; David, A. P. *J. Electrochem. Soc.* **1987**, *134*, 1389−1394.
(52) Centeno, T. A.; Stoeckli, F. *J. Power Sources* **2006**, *154*, 314−320.
(53) Lu, Y.; Xu, H.; Wang, J.; Kong, X. *Electrochim. Acta* **2009**, *54*, 3972−3978.
(54) Weininger, J. L.; Breiter, M. W. *J. Electrochem. Soc.* **1963**, *110*, 484−490.
(55) Weininger, J. L.; Breiter, M. W. *J. Electrochem. Soc.* **1964**, *111*, 707−712.
(56) O'Brien, R. N.; Seto, P. *J. Electroanal. Chem.* **1968**, *18*, 219−230.
(57) Hampson, N. A.; Latham, R. J.; Lee, J. B.; Macdonald, K. I. *J. Electroanal. Chem.* **1971**, *31*, 57−62.
(58) Gagnon, E. G. *J. Electrochem. Soc.* **1973**, *120*, 1052−1056.
(59) Lasia, A.; Rami, A. *J. Electroanal. Chem.* **1990**, *294*, 123−141.
(60) Gu, P.; Bai, L.; Gao, L.; Brousseau, R.; Conway, B. E. *Electrochim. Acta* **1992**, *37*, 2145−2154.
(61) Bai, L.; Gao, L.; Conway, B. E. *J. Chem. Soc., Faraday Trans.* **1993**, *89*, 235−242.
(62) Fournier, J.; Brossard, L.; Tilquin, J.-Y.; Cote, R.; Dodelet, J.-P.; Guay, D.; Menard, H. *J. Electrochem. Soc.* **1996**, *143*, 919−926.
(63) Wu, G.; Li, N.; Zhou, D.-R.; Mitsuo, K.; Xu, B.-Q. *J. Solid State Chem.* **2004**, *177*, 3682−3692.
(64) See Supporting Information.
(65) Conway, B. E.; Angerstein-Kozlowska, H. *Acc. Chem. Res.* **1981**, *14*, 49−56.
(66) Bard, A. J.; Faulkner, L. R. *Electrochemical Methods: Fundamentals and Applications*, 2nd ed.; John Wiley & Sons, Inc.: Hoboken, NJ, 2001, p 353−354.
(67) Prater, K. B.; Bard, A. J. *J. Electrochem. Soc.* **1970**, *117*, 207−213.
(68) Matsumoto, Y.; Sato, E. *Mater. Chem. Phys.* **1986**, *14*, 397−426.
(69) Another common metric by which to compare electrocatalysts is their Tafel parameters, including exchange-current density and Tafel slope. In this report, we chose not to use Tafel parameters as an activity metric due to the complexity in estimating and understanding the relevant parameters for multistep, multielectron transfer mechanisms. While Tafel plots are very useful for deriving mechanistic and kinetic information from specific electrocatalytic systems, we believe that determing relevant Tafel parameters for a given system is system specific and requires mechanistic analysis that is beyond the scope of this manuscript. For further discussion, please see the Supporting Information.
(70) Lu, P. W. T.; Srinivasan, S. *J. Electrochem. Soc.* **1978**, *125*, 1416−1422.
(71) McBreen, J. In *Modern Aspects of Electrochemistry*; Bockris, J. O. M., Conway, B. E., White, R. E., Eds.; Plenum: New York, 1990; Vol. *21*, p 29−63.
(72) Suntivich, J.; May, K. J.; Gasteiger, H. A.; Goodenough, J. B.; Shao-Horn, Y. *Science* **2011**, *334*, 1383−1385.
(73) Kuhl, K. P.; Cave, E. R.; Abram, D. N.; Jaramillo, T. F. *Energy Environ. Sci* **2012**, *5*, 7050−7059.
(74) McKone, J. R.; Sadtler, B. F.; Werlang, C. A.; Lewis, N. S.; Gray, H. B. *ACS Catalysis* **2012**, *3*, 166−169.
(75) Jiao, F.; Frei, H. *Energy Environ. Sci.* **2010**, *3*, 1018−1027.
(76) Surendranath, Y.; Kanan, M. W.; Nocera, D. G. *J. Am. Chem. Soc.* **2010**, *132*, 16501−16509.
(77) Yagi, M.; Tomita, E.; Kuwabara, T. *J. Electroanal. Chem.* **2005**, *579*, 83−88.
(78) Weber, M. F.; Dignam, M. J. *Int. J. Hydrogen Energy* **1986**, *11*, 225−232.
(79) Kishi, T.; Takahashi, S.; Nagai, T. *Surf. Coat. Technol.* **1986**, *27*, 351−357.
(80) Laouini, E.; Hamdani, M.; Pereira, M. I. S.; Douch, J.; Mendonça, M. H.; Berghoute, Y.; Singh, R. N. *Int. J. Hydrogen Energy* **2008**, *33*, 4936−4944.
(81) Guerrini, E.; Chen, H.; Trasatti, S. *J. Solid State Electrochem.* **2007**, *11*, 939−945.
(82) Morimitsu, M.; Murakami, C.; Kawaguchi, K.; Otogawa, R.; Matsunaga, M. *J. New Mater. Electrochem. Syst.* **2004**, *7*, 323−327.
(83) Pourbaix, M. *Atlas of Electrochemical Equilibria in Aqueous Solution*; Pergamon Press: Oxford, 1966, p 373−377.
(84) Trotochaud, L.; Mills, T. J.; Boettcher, S. W. *J. Phys. Chem. Lett.* **2013**, *4*, 931−935.